



Alternating zonal jets and energy fluxes in barotropic wind-driven gyres

B.T. Nadiga^{a,*}, D.N. Straub^b

^a Los Alamos National Lab., MS-B296, Los Alamos, NM 87545, United States

^b McGill Univ., Burnside Hall 819, 805 Sherbrooke West Montreal, Que., Canada H3A 2K6

ARTICLE INFO

Article history:

Received 27 October 2009

Received in revised form 7 January 2010

Accepted 20 February 2010

Available online 10 March 2010

Keywords:

Ocean circulation

Alternating zonal jets

Wind-driven circulation

Energy flux

ABSTRACT

The barotropic β -plane vorticity equation is considered under steady large scale (double-gyre) and small scale (stochastic) forcing. For both forcings, regimes are found in which alternating zonal jets appear. For steady large scale forcing, this regime is characterized by weak forcing and weak dissipation. Attention is focused on energy cascades due to the nonlinear and β terms and the jets are found to be associated with to a near compensation in these cascades over a range of wavenumbers. Additionally, interaction between flow forced at large scale and flow forced at small scale is examined.

Published by Elsevier Ltd.

1. Introduction

Recent evidence has unmasked the presence of alternating zonal jet-like features superimposed on the larger scale mid-latitude oceanic gyre circulation (Treguier et al., 2003; Nakano and Hasumi, 2005; Maximenko et al., 2005; Richards et al., 2006; Maximenko et al., 2008). While the exact mechanism underlying the formation of these features is still not well understood, a number of possible mechanisms have been suggested. For example, alternating jets are well-known from β -plane turbulence and are associated with a halting of the two-dimensional inverse energy cascade by Rossby wave dispersion (e.g., Rhines, 1975; Vallis and Maltrud, 1993; Panetta, 1993). Thus, it is possible that the recently observed features are consistent with the classic picture of ocean energetics whereby barotropization of mesoscale eddies acts as an effective small scale energy source for the barotropic flow (e.g., Salmon, 1998; Vallis, 2006). A subsequent inverse energy cascade to the Rhines scale would then produce the jets.

However, the reflection of long Rossby waves as short Rossby waves at a western boundary and the attendant inviscid generation of anisotropy can lead to dynamics that are different from those in the zonally periodic setting. For example, in the case with meridional boundaries, a linear forward cascade of energy, associated with the β term, is possible, whereas that is not the case in a periodic setting. Nevertheless, idealized numerical studies (Kramer et al., 2006; Nadiga, 2006) in a closed basin suggest that the anisot-

ropization-of-inverse-cascade mechanism can survive in the presence of meridional boundaries, as is relevant for the oceanic context. Other suggestions for the formation of oceanic jets include nonlinear self-interactions of linear eigenmodes (Berloff, 2005; Berloff et al., 2009) and that such jets are preferred growing structures excited by the imposed stochastic forcing (Farrell and Ioannou, 2007). Finally, zonal jets can be formed simply by the instability of barotropic Rossby waves (Lorenz, 1972; Gill, 1974; Connaughton et al., in press).

Both the β -plane turbulence and the gyre scale dynamics are nonlinear and it seems reasonable to anticipate that the two will interact. A full description of the interactions will clearly necessitate consideration of baroclinic effects; it nonetheless seems useful to begin by understanding how jets interact with the wind-driven circulation in the simpler context of the purely barotropic problem. In this paper, we consider the β -plane barotropic vorticity equation in a box geometry forced by (i) a steady large scale wind, (ii) a small scale stochastic forcing and (iii) both. The first case is the classic mid-latitude double gyre problem. The second has previously been used to model the jets (Nadiga, 2006; Kramer et al., 2006). It might be thought of as a crude model of energy being injected by small scale baroclinic eddies into the barotropic mode. The third allows us to consider interactions between the two. We focus primarily on a description of the energy cascades.

In Section 2, we describe the model and introduce diagnostics. Section 3 gives results for the three types of forcing. We first describe a regime in which jets appear in the barotropic double gyre problem. The jets are shown to be associated with a near compensation between a (linear) forward energy cascade related to the β effect in the presence of meridional boundaries and the nonlinear

* Corresponding author.

E-mail addresses: balu@lanl.gov (B.T. Nadiga), david.straub@mcgill.ca (D.N. Straub).

inverse cascade familiar from two-dimensional turbulence. Next, consistent with previous studies, we also find jets to appear in response to small scale stochastic forcing. Note that in both cases, the jets are visible only after averaging. In instantaneous snapshots, they are masked by the presence of a stronger isotropic eddy field. Finally, interaction between flow forced at small and large scale is considered. A discussion in Section 4 is then followed a brief summary in Section 5.

2. Model, diagnostics and background

2.1. Equations, parameters and diagnostics

We solve the barotropic quasigeostrophic potential vorticity equation:

$$\begin{aligned}\frac{\partial q}{\partial t} &= -J(\psi, q) + F - r\nabla^2\psi + A\nabla^8\psi \\ q &= \nabla^2\psi + \beta y\end{aligned}\quad (2.1)$$

The model domain is taken to be a square box of width $2\pi L$. Forcing, F , includes a large scale wind forcing $F_{\text{large}} = F_0 \sin(y/L)$ and a small scale stochastic forcing, F_{small} . F_{small} injects energy at a average rate, ϵ , into a narrow ring of wavenumbers centered on a large wavenumber, k_f . This forcing is stochastic in time spatially homogeneous and present in a narrow ring of wavenumbers centered around a k_f of 128. Time dependence in F_{small} is given by an Ornstein–Uhlenbeck process. The decorrelation time corresponds to about 4% of an estimate of the turnover time, L/U_{rms} . A consequence of this choice is that ϵ is not known *a priori*, but must be measured. We have conducted a few of the stochastically forced simulations with white noise forcing instead of the colored forcing and verified that our results remain the same. At lateral boundaries, a generalization of slip conditions appropriate for hyperviscosity is applied. Specifically, we set $\nabla^2\psi = \nabla^4\psi = \nabla^6\psi = 0$. With this choice, boundary terms that might otherwise appear in the energy equation are eliminated.

An equation for the domain-averaged energy, E , is found by multiplying (2.1) by ψ and averaging over the domain:

$$\frac{dE}{dt} = \text{Forcing} - 2rE - \frac{A}{4\pi^2L^2} \int \int (\nabla^4\psi)^2 dx dy. \quad (2.2)$$

Here, the forcing term is the sum of the energy injection rate due to the small scale stochastic forcing and W , the wind power source. W is given by

$$W \dot{=} \frac{-1}{4\pi^2L^2} \int \int (\psi F_{\text{large}}) dx dy. \quad (2.3)$$

In the absence of a forward energy cascade to dissipation wavenumbers, energy dissipation by the hyperviscosity is negligible and statistical equilibrium implies

$$2r\bar{E} = rU_{\text{rms}}^2 \approx \epsilon + \bar{W}, \quad (2.4)$$

where overbars denote time averages.

As mentioned, ϵ must be determined from the solution since the stochastic forcing used had a finite decorrelation time. Similarly, \bar{W} is also a function of the solution; however, one can make a useful *a priori* estimate by assuming the large scale flow to be well approximated by the Sverdrup balance:

$$\beta \frac{\partial \psi_{\text{sv}}}{\partial x} = F_{\text{large}}. \quad (2.5)$$

This gives

$$\bar{W} \approx \frac{F_0^2 \pi L}{2\beta}, \quad (2.6)$$

which is a good approximation, except where damping is weak, in which case a four gyre response tends to develop and \bar{W} decreases (Greatbatch and Nadiga, 2000). Note that (2.4) and (2.6) yield an estimate for the root mean square (rms) velocity at statistical equilibrium.

In general, the problem is defined by the dimensional parameters $\beta, L, F_0, \epsilon, k_f, r$ and A . The precise value of A is largely irrelevant. The main role of hyperviscosity is to damp enstrophy variance, which cascades forward to high wavenumbers and the value of A determines the position of a viscous tail in the spectra. Although bottleneck effects can influence the spectra at wavenumbers slightly to the left of the viscous tail (e.g., see Frisch et al., 2008), for sufficiently high resolution (and low A), the spectra are insensitive to A over low-to-moderate wavenumbers. We choose $k_f = 128$, so that k_f^{-1} is small compared to 1 and large compared to the viscous scale. To limit the size of our parameter space, k_f, L, A and β will be held fixed.

A range of values for the remaining parameters, r, F_0 and ϵ will be considered. It is convenient to express these non-dimensionally. Consider first the case with large scale forcing only. It is common in oceanography to express r and F_0 non-dimensionally as (e.g., Pedlosky, 1996):

$$\delta_s \equiv \frac{r}{\beta L}, \quad \delta_i \equiv \frac{F_0^{1/2}}{\beta L}. \quad (2.7)$$

Physically, δ_s and δ_i give the ratio of the linear Stommel layer thickness and an *a priori* estimate of the inertial boundary layer thickness to L .¹ Note that $L\delta_i$ can be thought of as a Rhines scale,

$$\delta_i = \frac{1}{L} \left(\frac{U_{\text{sv}}}{\beta} \right)^{1/2}, \quad (2.8)$$

where $U_{\text{sv}} = F_0/\beta$ gives the Sverdrup velocity amplitude. Alternatively, one might wish to consider a Rhines scale based on an estimate of the rms velocity. Taking $\epsilon = 0$ and using (2.4) and (2.6), we define

$$\delta_l \dot{=} \delta_i \left(\frac{\pi}{2\delta_s} \right)^{1/4} \approx \left(\frac{U_{\text{rms}}}{\beta L^2} \right)^{1/2}. \quad (2.9)$$

Loosely speaking, δ_l might be thought of as giving an estimate of the energy-containing eddy scales in the gyre problem. In eddying flows, typically, δ_l is larger than δ_i .

Given the form of (2.9), it is obvious that the same δ_l can be achieved by different combinations of forcing δ_i and dissipation δ_s . Moreover, one might anticipate a difference in behavior between, for example, a case where δ_l is made large by choosing δ_i large and one where the same δ_l is achieved by choosing δ_s small. One of our principal findings is that, in the latter case (dissipation and forcing both small), zonal jets appear super-posed on the double gyre circulation. To our knowledge, this is the first time jets have been produced in a gyre simulation with neither baroclinity nor small scale forcing.

By analogy with δ_l , we can also define a similar parameter for the small scale forcing:

$$\delta_\epsilon \dot{=} \frac{1}{L} \left(\frac{\epsilon}{\beta^2 r} \right)^{1/4} \approx \left(\frac{U_{\text{rms}}}{\beta L^2} \right)^{1/2}, \quad (2.10)$$

where in this case, $U_{\text{rms}} \approx (\epsilon/r)^{1/2}$. For a simulation forced by F_{small} , one expects an inverse cascade feeding energy into zonal jets with a characteristic width that scales like δ_ϵ . This assumes, of course, that the Rayleigh damping is sufficiently weak so as to allow the inverse energy cascade to reach the Rhines scale, which will typically be the case if δ_s is small compared to δ_ϵ .

¹ Note that Pedlosky's definition differs from ours by a factor of 2π .

To recap, δ_s , δ_e and δ_l (or δ_i) define three independent length-scales, non-dimensionalized by L . δ_s gives the linear Stommel boundary layer width and δ_e and δ_l are Rhines scales based on the expected rms velocity associated with F_{small} and F_{large} , respectively.

2.2. Numerical model

The domain is discretized with 1025 grid points on a side to give a $\delta_x = \Delta x/L$ of $6.14e - 3$. Eq. (2.1) is finite differenced using the Arakawa discretization (Arakawa, 1966) for the Jacobian and centered differencing for the spatial discretization of the other terms. Such a discretization of the Jacobian ensures that the advective fluxes are exactly energy and enstrophy conserving in the absence of forcing and dissipation. The time stepping is carried out using an adaptive, (nominally) fifth order, embedded Runge–Kutta Cash–Karp scheme [(Press et al., 1986)]. In addition to providing better time accuracy compared to the usual leapfrog time discretization, this forward-time discretization obviates the need for time-filtering used to remove the computational mode in the leapfrog discretization. This combination of spatial and temporal discretization leads to a robust nonlinearly stable model. Finally, the slip conditions were applied by simply setting $\nabla^2\psi = \nabla^4\psi = \nabla^6\psi = 0$ at boundaries.

2.3. Energy diagnostics

A spectral version of the energy equation can be written as

$$\frac{\partial}{\partial t}E(k, t) \approx T(k, t) + \epsilon(k) + W(k, t) - 2rE(k, t), \quad (2.11)$$

where $k = (k_x^2 + k_y^2)^{1/2}$ is horizontal wavenumber and energy dissipation associated with the hyperviscous term is neglected. Integrating over k , one recovers (2.2) and then time averaging gives (2.4).

T represents transfers between the wavenumbers. It integrates to zero and can be further broken down into its nonlinear and β components:

$$T(k, t) = T_\beta(k, t) + T_N(k, t). \quad (2.12)$$

Recall that the energy equation comes from multiplying (2.1) by ψ and integrating. In calculating the various terms in (2.11), we first take the sine transforms of ψ and various terms on the right hand side of (2.1), e.g., $-\beta\psi_x$, $-J(\psi, \nabla^2\psi)$, etc. Then, denoting the transforms by hats and the complex conjugate by an asterisk,

$$T_\beta(k, t) = \frac{\beta}{4\pi^2 L^2} \int \int \Re(\hat{\psi}^* \hat{\psi}_x) dk_x dk_y, \quad (2.13)$$

in which $\Re()$ denotes ‘real part of’ and the x subscript on $\hat{\psi}$ denotes partial differentiation. Other terms in (2.12) are defined similarly. Note that $\hat{\psi}_x$ is the sine transform of the x derivative of ψ , not the x derivative of the sine transform of ψ . The two, of course, represent the same physical field; however, the representation is different (i.e., use of sine rather than cosine functions).

Since we are interested in the statistical equilibrium, we will take time averages. For example, $W(k)$, $T(k)$ and $E(k)$ are time averages of $W(k, t)$, $T(k, t)$ and $E(k, t)$ at statistical equilibrium. We will also be interested in the flux of energy, $\Pi(k)$, through a given wavenumber, k :

$$\Pi(k) = - \int_0^k T(k') dk' = \int_k^\infty T(k') dk'. \quad (2.14)$$

Positive Π corresponds to a forward transfer through k to higher wavenumber and as before, we can break up Π into its nonlinear and β components (Π_β and Π_N). For k smaller than k_f , F_{small} vanishes and

$$\Pi(k) = W(k) - 2rE(k), \quad (2.15)$$

where $E^<(k)$ is the energy at scales larger than k^{-1} . Note that $E^<(k)$ is a positive monotonically increasing function of k . Because $W(k)$ is localized at small k , beyond about wavenumber three or so, $W^<(k)$ can be considered essentially constant. Equivalently, for $k < k_f$, but larger than the wavenumbers where W is active,

$$\Pi(k) = -\epsilon + 2rE^>(k), \quad (2.16)$$

where $E^>(k)$ is the energy at scales smaller than k^{-1} .

3. Results

We report a total of 10 experiments covering a range of our parameter space, Table 1. The first six use large scale (gyre) forcing only. We consider two values for δ_l and different combinations of δ_i and δ_s for each δ_l . These experiments are described in Section 3.1. Following that, two cases for which only small scale (jet) forcing was used (Section 3.2) and two with both large and small scale forcing (Section 3.3) are presented.

3.1. Gyre forcing: F_{large}

We begin by considering the weakly nonlinear case, G1, for which δ_s and δ_l are comparable, although δ_l is slightly larger. Fig. 1a shows the time-averaged streamfunction. Away from the western boundary and except for a small region near the confluence of the two boundary currents, $\bar{\psi}$ strongly resembles the classic Sverdrup solution. Shown in Fig. 1b are the spectral fluxes. Π is seen to be dominated by Π_β , which shows a forward cascade of energy between about wavenumbers 2 and 20. The cascade then tapers off to zero between wavenumbers 20 and 200. The lower curve in the figure corresponds to a mirror image of the right hand side of (2.15), i.e., to $-(W^<(k) - 2rE^<(k))$. Consistent with (2.15), this closely mirrors $\Pi(k)$: the residual is small by comparison. Scale selective dissipation is also included; however, this plays only a minor role.

Fig. 2 further decomposes the lower curve in Fig. 1b into its forcing and dissipation components. As anticipated, $W^<(k)$ increases quickly to a near-constant value, confirming that the forcing projects mainly onto a few low wavenumbers. By contrast, $-2rE^<(k)$ first decreases slowly at low wavenumbers and then more rapidly in the energy containing scales. Consequently, Π is relatively flat where $2rE^<(k)$ remains small with respect to $W^<(k)$, and then drops off rapidly in the energy-containing scales, where dissipation via Rayleigh drag reduces the amount of energy that must be transferred forward through a given wavenumber. Note that the k axis uses a log scale. Therefore, the slope in Π is proportional to $kE_{2d}(k)$ (for k large enough such that $W^<(k)$ is constant). Also evident from the figure is that, as expected, hyperviscous

Table 1

Non-dimensionalized parameters considered. δ_l is a measure of steady large scale gyre forcing, δ_s is a measure of Rayleigh friction, and δ_i is a measure of the energy containing scale and is related to (large scale) forcing and dissipation. δ_e is the corresponding measure of the energy-containing scale for cases with stochastic small scale forcing.

Run #	δ_l	δ_i	δ_s	δ_e
G1	1.41e – 2	5.59e – 3	6.25e – 3	0
G2	2.97e – 2	1.18e – 2	6.25e – 3	0
G3	2.97e – 2	5.59e – 3	3.13e – 4	0
G4	2.97e – 2	2.79e – 3	1.95e – 5	0
G5	1.41e – 1	5.59e – 2	6.25e – 3	0
G6	1.41e – 1	5.59e – 3	6.18e – 7	0
J1	0	0	3.13e – 4	1.83e – 1
J2	0	0	3.13e – 4	3.86e – 1
G3J1	2.97e – 2	5.59e – 3	3.13e – 4	1.85e – 1
G3J2	2.97e – 2	5.59e – 3	3.13e – 4	3.86e – 1

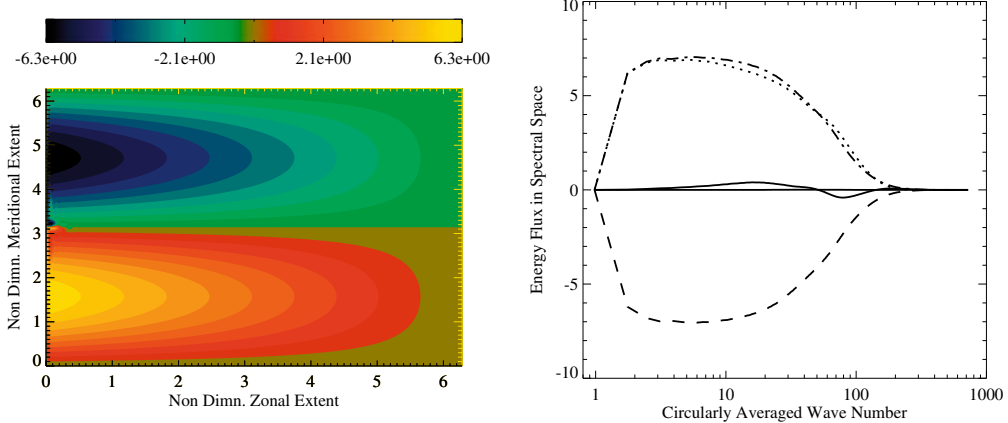


Fig. 1. Time-averaged fields for experiment G1: streamfunction (left) and spectral fluxes (right). Shown are the total flux, Π (dot-dashed line), its components Π_β (dotted line) and Π_N (solid line) as well as the (negative of) the flux due to forcing and dissipation (dashed line) and the residual (dot-dot-dot-dashed line).

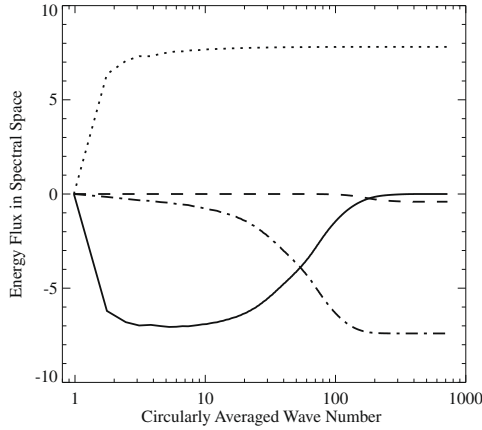


Fig. 2. Further decomposition of the forcing and dissipation spectral flux at equilibrium for experiment G1 due to : forcing (W^c , dotted-line). Note that $W^c = W * 4 * \pi^2$ Rayleigh drag ($-2rE^c$, dot-dashed line) and small-scale dissipation (dashed line). Also shown is the negative of their sum (cf. Fig. 1).

energy dissipation is evident only at high wavenumbers and remains small with respect to the Rayleigh term everywhere.

It is interesting to compare Π to its analog, Π_{Stommel} for the classic (linear, steady) Stommel double gyre solution. Given the similarity between the classic Stommel solution and the $\bar{\psi}$ field in Fig. 1a, one expects the two fluxes to be similar. On the other hand, one might also anticipate that Π_{Stommel} would show a cascade to a much larger wavenumber, e.g., to a k on the order of $k \sim \delta_s^{-1}$, here about 160. That is, one anticipates that the cascade should proceed to the energy-containing scales at which dissipation occurs, and that for the Stommel gyre this corresponds to the inverse of the Stommel boundary layer width. From Fig. 1b, Π begins tapering off at a much lower wavenumber. We calculated Π_{Stommel} both numerically and analytically and found it to very closely resemble Π in Fig. 1b. Somewhat counter-intuitively, the energy spectrum for Stommel's solution has a maximum at its gravest non-zero wavenumber and then plateaus off to a near-constant value out to a wavenumber related to the inverse Stommel boundary layer width. Thus, consistent with expectation, the energy-containing scales – large $kE(k)$ – are concentrated at a large wavenumber. Specifically, $kE(k)$ has a maximum at about $k\delta_s = 1/\sqrt{3}$, or about $k \approx 93$ for our parameters. However, the peak in $kE(k)$ is sufficiently broad so that Π begins to drop off its plateau at a relatively low wavenumber ($k \sim 20$), as in Fig. 1b. Details of the calculation for the linear Stommel problem are given in the Appendix A.

An overall picture of the energetics in the weakly forced case, G1, is that W inputs energy near $k = 1$ and the β term transfers energy forward to the energy-containing scales of the spectrum, where it is removed by the Rayleigh drag. Nonlinear and hyperviscous terms play lesser roles by comparison. We will see below that as the Rayleigh friction coefficient is reduced, Π_β increases at intermediate values of k . Moreover, instead of tapering off in association with Rayleigh drag, it feeds a nonlinear inverse cascade (see, e.g., Fig. 4).

Experiments G2 and G3 show results for a larger δ_l . Note that G2 has the same δ_s as does G1, whereas G3 has the same δ_l . That is, in going from G1 to G2, δ_l was increased by increasing the forcing and in going from G1 to G3, it was increased by decreasing the Rayleigh drag. Figs. 3 and 4 show the results.

Comparing Fig. 3 to Fig. 1, we see that the time averaged streamfunction is much as before, except that the region of nonlinearity near the confluence is somewhat larger and more energetic, as one might expect. Instantaneous snapshots show strong nonlinearity over a much larger portion of the domain as well. (The ratio $U_{\text{rms}}/U_{\text{Sv}}$ is approximately 6.4.) In the transfers, the main differences with respect to Fig. 1 are that Π_N is somewhat larger than before (although it remains small) and the β flux does not proceed as far as previously. Note also that Π_N tends to act in the opposite sense as Π_β over the energy-containing scales and that the net forward energy flux begins to taper off at smaller k than previously, e.g., beyond about wavenumber 10. In a sense, this is not surprising: after all, δ_l is larger in Experiment G2 and Rayleigh dissipation is most active in the energy-containing scales. On the other hand, it is counter-intuitive that the more strongly forced case (G2) appears to distribute its energy over fewer degrees of freedom than does G1, for which the energy cascade proceeds to higher wavenumber. The apparent paradox is resolved when one considers the two-dimensional spectra. That is, although energy resides at larger wavenumbers in G1, there is also a stronger anisotropy, with more energy in zonal (k_x) than meridional (k_y) wavenumbers. This anisotropy is reduced in G2 (not shown). In other words, because in G1 energy is concentrated in a narrow band of k_y , the longer forward cascade seen in that experiment does not imply a distribution of energy over a large number of Fourier modes.

Fig. 4 shows a more interesting nonlinear behavior. In addition to an eddy rich region near the boundary current confluence, zonal jets appear in the time averaged $\bar{\psi}$ field. To better visualize the jet structure, Fig. 5 shows the time averaged zonal velocity field, following a spectral filtering to remove the gravest k_y modes (i.e., the Sverdrup gyres). Note also that the jets are particularly strong adjacent to the northern and southern boundaries. Also shown in the Fig. 5 is a twin experiment, but for which the north-

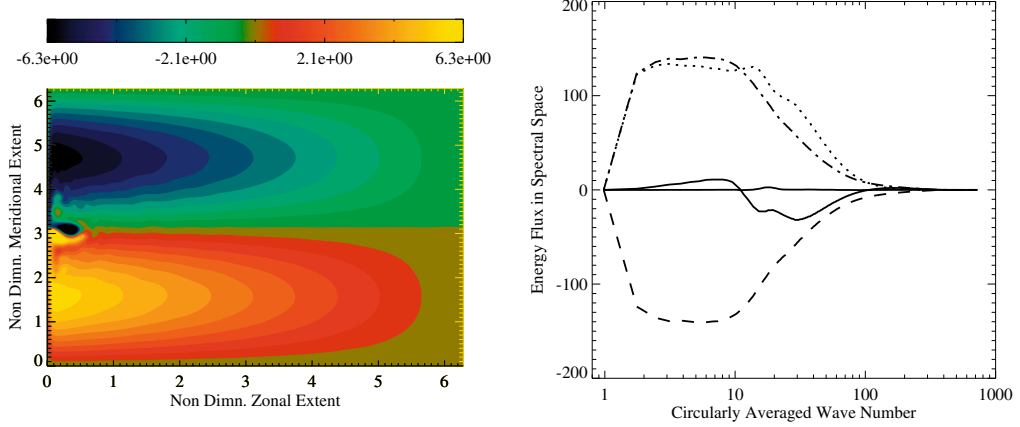


Fig. 3. Time-averaged streamfunction and spectral fluxes for experiment G2. Conventions are the same as in Fig. 1. In going from case G1 to G2, the forcing was increased to attain a larger value for δ_l . $\delta_s = 6.25e - 3$, $\delta_i = 1.18e - 2$, $\delta_l = 2.97e - 2$

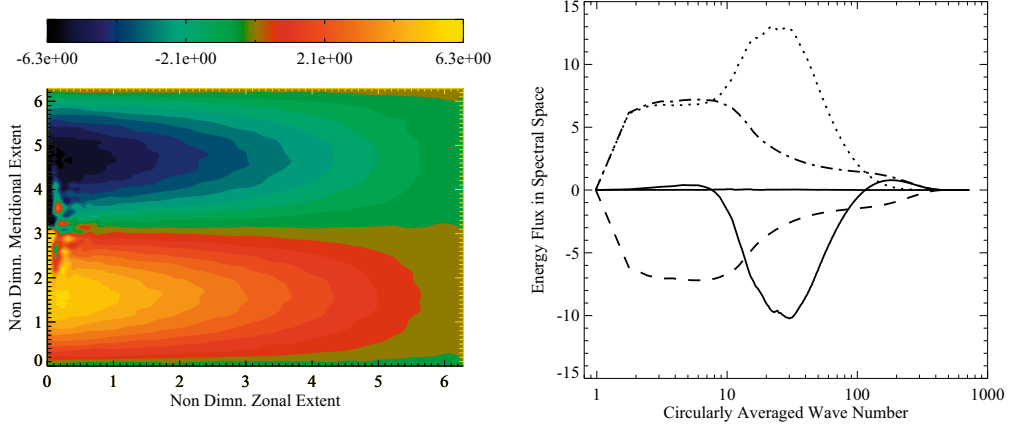


Fig. 4. Time-averaged streamfunction, zonally averaged zonal velocity (center) and spectral fluxes for experiment G3. Conventions are the same as in Fig. 1. In going from case G1 to G3, Rayleigh friction was decreased, while holding the forcing fixed, to attain a larger value for δ_l . $\delta_s = 3.13e - 4$, $\delta_i = 5.59e - 3$, $\delta_l = 2.97e - 2$. The compensating β and nonlinear fluxes is a characteristic signature of the alternating zonal jets.

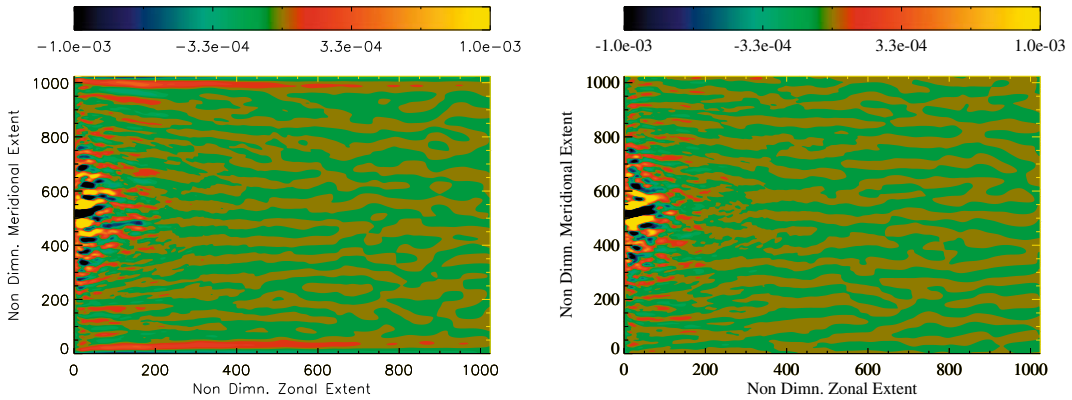


Fig. 5. Long time averages of the streamfunction after removing the $\sin(y)$ component of ψ (i.e., so that the gyres are filtered out). Outside of the jet-confluence region near the western boundary, alternating jets are clearly visible. The left panel corresponds to experiment G3 and right panel corresponds to a similar experiment, but for which a periodicity in y was imposed to remove effects relating to the zonal (northern and southern) boundaries, e.g., so that the strong jets along the northern and southern boundary are absent. The twin experiment demonstrates (see later discussion) that the dynamics of the jets in the interior are not slaved to those of the strong jets at the northern and southern boundaries.

ern and southern walls are replaced by an imposed periodicity in y (see discussion below). For both Figs. 4 and 6, the averaging period was about 20 large scale turnover times, defined as L/U_{Sv} , where L is the basin width divided by 2π and U_{Sv} is the Sverdrup velocity amplitude. For such a long averaging period, results were insensi-

tive to the length of the averaging period. This is discussed further in the discussion section.

To our knowledge, this is the first time jets have been seen this distinctly in the barotropic double gyre problem. Note that the jets appear only in time averaged fields; in snapshots there are masked

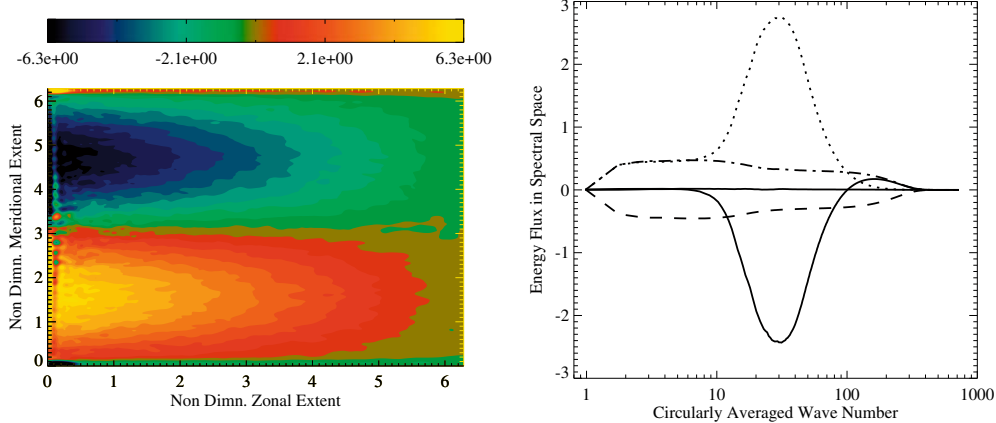


Fig. 6. In experiment G4, a lowering of both the forcing and Rayleigh friction enhances the importance of the alternating zonal jets. The associated compensating β and nonlinear fluxes similarly grow in magnitude. $\delta_s = 1.95e-5$, $\delta_i = 2.79e-3$, $\delta_l = 2.97e-2$.

by the eddy field. The fluxes in Fig. 4 also show an interesting behavior. Although much as in G2, Π starts to taper off beyond about $k = 10$, the individual components Π_β and Π_N are active at much higher wavenumbers. Between about wavenumbers 7 and 100, Π_N shows an upscale energy transfer that is largely balanced by an increased forward transfer by the β term. Essentially, the β term cascades energy forward and the nonlinear term brings it back, with the Rayleigh drag providing the dissipation mechanism. The net result is a more interesting behavior, including the appearance of zonal jets.

The jets become increasingly evident in the weakly forced, weakly dissipated limit. For example, G4 is a more extreme version of G3, having the same δ_l , but weaker forcing and weaker Rayleigh damping. The time averaged streamfunction (Fig. 6) shows strong jets superimposed on the Sverdrup gyres. Additionally, small scale eddies also appear in the time mean near the western boundary.

Also shown in Fig. 6 are the fluxes. Once again, there are large and nearly compensating Π_β and Π_N cascades out to about $k = 100$. Note that this near compensation occurs not only in the fluxes (which are integrals of the transfers), but also in the transfers themselves. That is, except for the sign, the two-dimensional nonlinear and β transfers plotted as functions of k_x and k_y for G4 show nearly identical structures over the range of wavenumbers corresponding to the near-compensation in Π_β and Π_N (not shown).

Note also that in this simulation the forcing and dissipation terms are significantly smaller than the nonlinear terms. One

might therefore anticipate a tendency towards potential vorticity homogenization. For example, it might be argued that the jets result from an incomplete mixing of potential vorticity into a staircase pv profile. This does not turn out to be the case, however. For example, in Experiment G6 – where the forcing and dissipation terms are much smaller than the nonlinear terms – the jets persist and homogenization does not occur. That is, except adjacent to the boundaries, meridional profiles of time averaged potential vorticity are dominated by the $\beta\bar{y}$ term.

Finally, a third (larger) value of δ_l is considered in G5 and G6. Relative to G1, F_0 is increased for G5 and the Rayleigh drag is decreased for G6. Note that these differences are large: F_0 in G5 is 100 times its value in G1 and the drag coefficient is reduced by about four orders of magnitude between G1 and G6. Results are shown in Figs. 7 and 8. In Fig. 7, the G5 \bar{y} field shows a pattern familiar to oceanographers, with two strong inertial recirculations distorting the background Sverdrup gyres. Interestingly, the role of the nonlinear term relative to that of the β term is reduced compared, say, to G3. That is, Π_N remains relatively small compared to Π_β . Note also that the total cascade, Π , begins tapering off strongly just beyond about wavenumber three. In other words, although G5 is strongly nonlinear, the system in a sense uses only a small fraction of the degrees of freedom (i.e., wavevectors) available to it. Fig. 8 shows essentially an exaggerated version of what we saw for G4. Note also the appearance of strong inertial recirculations along the northern and southern boundaries. It should also

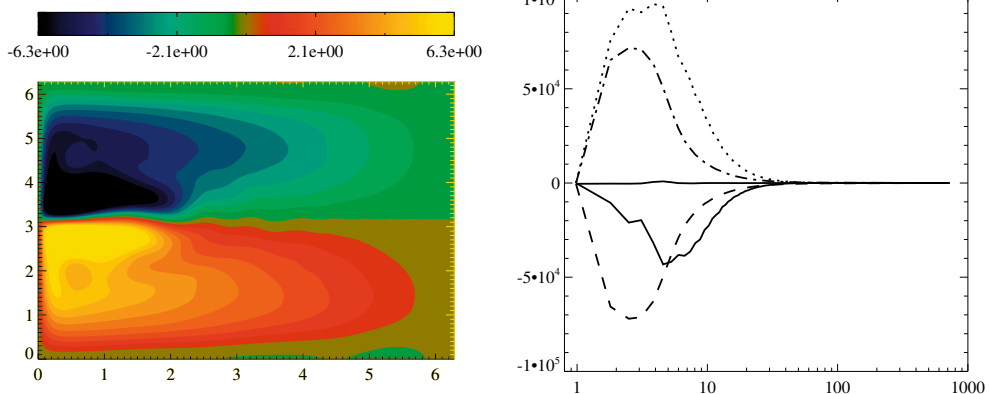


Fig. 7. In experiment G5, Rayleigh friction is held the same as in G1 and G2, but the forcing is increased further, as in G2, but only more so. The result is the formation of the familiar recirculation gyres at the jet-confluence region. Note, that in this case, the nonlinear flux is smaller than the forcing and dissipation flux. The nonlinear flux is smaller than the β flux unlike in the cases where jets form. $\delta_s = 6.25e-3$, $\delta_i = 5.59e-2$, $\delta_l = 1.41e-1$.

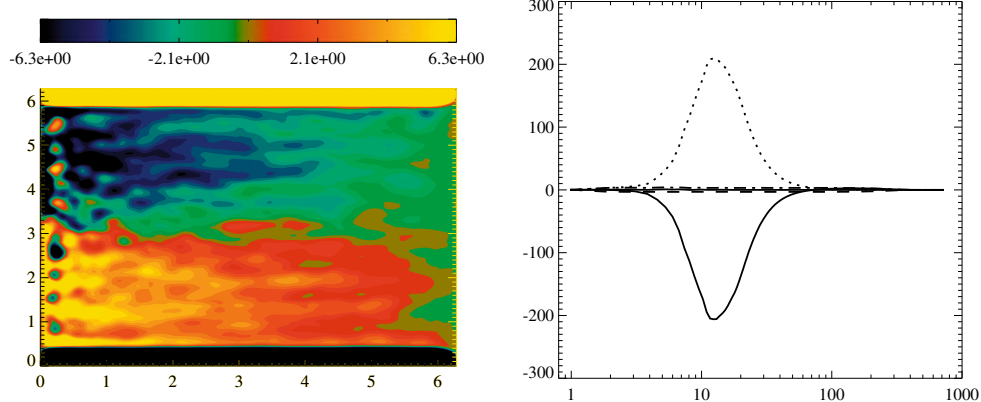


Fig. 8. Experiment G6 is in the same sense as going from G1 to G3. However, Rayleigh friction is further decreased. $\delta_s = 6.18e - 7$, $\delta_i = 5.59e - 3$, $\delta_l = 1.41e - 1$. The alternating jets and their associated spectral fluxes begin to dominate. An experiment similar to G3-twin experiment confirms that the characteristics of the jets in the interior are not modified to the leading order by the strong jets at the northern and southern boundaries.

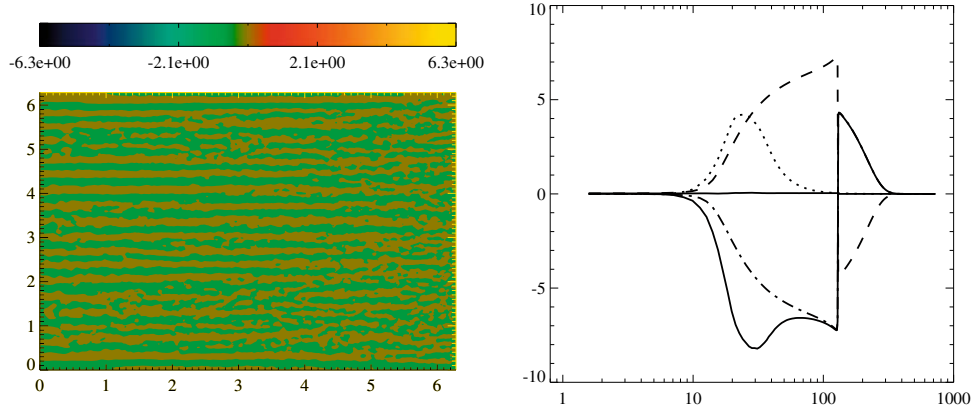


Fig. 9. In experiment J1, a small scale isotropic stochastic forcing is used, resulting in alternating zonal jets like in Nadiga (2006). Superposed over the inverse cascade is the compensating β and nonlinear flux characteristic of the zonal jets. $\delta_s = 3.13e - 4$, $\delta_e = 1.83e - 1$.

be pointed out that the Rayleigh drag in G6 is so weak that energy dissipation is actually accomplished by the hyperviscous term. The results for this experiment, then, are presumably sensitive to the hyperviscous coefficient, A , and as such non-generic.

As noted, the zonal jets have their strongest expression at the northern and southern walls. In order to verify the possible dependence of the jets on the presence of the zonal boundaries at the

northern and southern limits of the domain, we repeated experiments G3, G4 and G6 by imposing periodicity in the streamfunction and relative vorticity fields across the northern and southern boundaries. In such a setup, the absence of solid walls at the northern and southern limits of the domain does not allow for the meridional pressure gradients that support strong zonal jets. In these experiments we find that the structure and strength of the

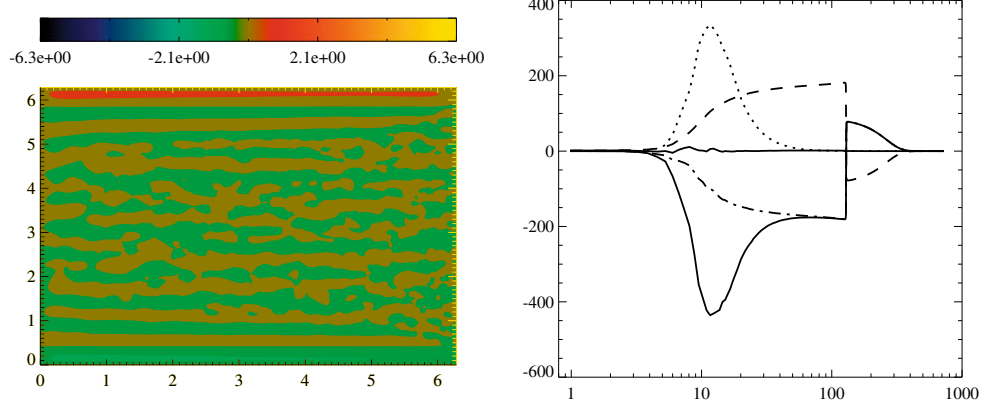


Fig. 10. A stronger stochastic forcing in experiment J2 produces a fewer number of stronger jets. The spectral signature of the jets is correspondingly stronger. $\delta_s = 3.13e - 4$, $\delta_e = 3.86e - 1$.

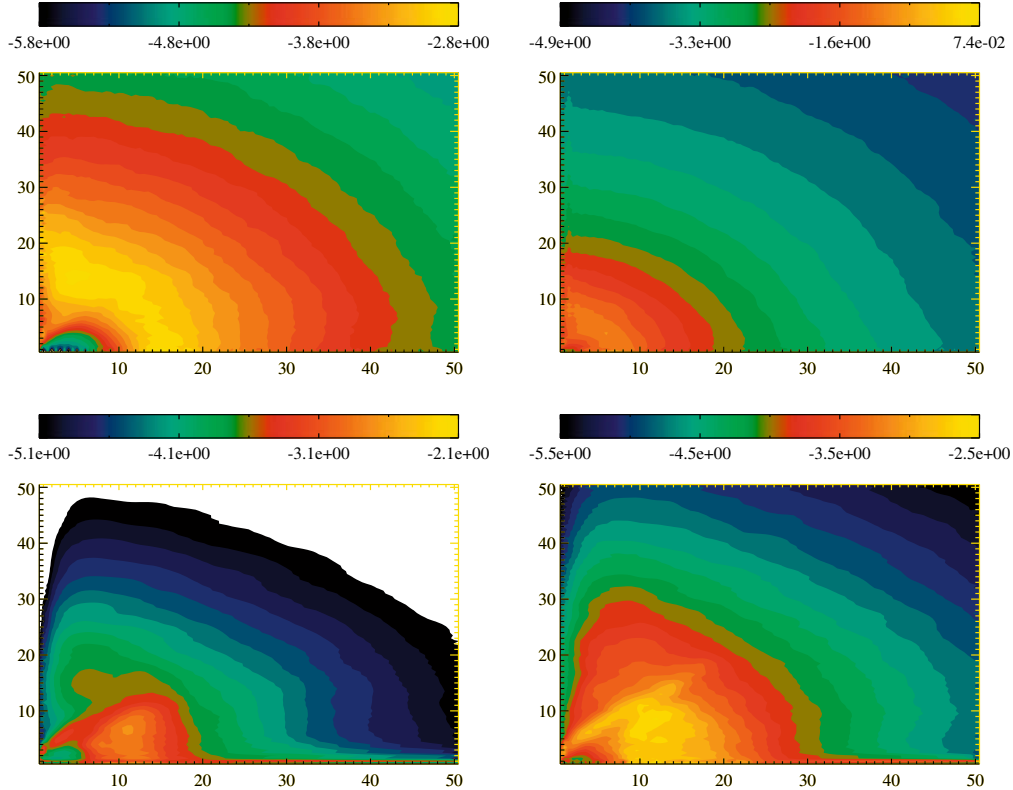


Fig. 11. Two-dimensional energy spectra: J1 (top left), J2 (top right), G3 (bottom left) and G4 (bottom right). The excluded dumbbell region at low wavenumbers is evident in case J1, whereas this region is barely visible in case J2. Similar excluded regions are visible in the gyre cases. However, in these cases there is stronger anisotropy at larger wavenumbers, with significant energy along $k_y = 1$. The streaks along the $k_x \sim k_y$ direction in the gyre cases are associated with Rossby waves that are oriented at roughly 45° to the meridional in physical space.

jets in the interior are very similar to those shown and discussed for cases G3, G4 and G6. (The jet structure evident on removing the gravest meridional modes for the case corresponding to case G3 is shown on the right side panel in Fig. 5.) This suggests that the formation and characteristics of the zonal jets in the interior are not strongly dependent on the presence of impenetrable walls at the northern and southern limits of the domain.

3.2. Stochastic forcing: F_{small}

We have seen in the previous section that alternating zonal jets can arise in response to purely large-scale and steady wind forcing and that these jets are associated with a compensating beta and nonlinear flux of energy. However, as mentioned in the introduction, the occurrence of alternating zonal jets in the presence of small scale stochastic forcing is well-known from β -plane turbulence. That this mechanism can survive in the presence of meridional boundaries is demonstrated in Kramer et al. (2006) and Nadiga (2006). Here we analyze the spectral fluxes associated with such small-scale forced jets. Two experiments, J1 and J2, were carried out. Both have δ_s as in G3 and J2 corresponds to a more strongly forced case than does J1. Results are shown in Figs. 9 and 10.

In both experiments, the presence of alternating zonal jets is evident in the time mean fields. As is evident in the plots of spectral fluxes, in both cases J1 and J2, the forcing was applied at wave-number 128 and there is significant range of scales over which there is inverse cascade before the appearance of jets. In J1 these are relatively weak and in the more strongly forced J2, they are stronger and wider. Note that a fraction of the energy input by the stochastic forcing is directly dissipated by small scale dissipa-

tion. Similarly, a fraction of the enstrophy input inverse cascades and is dissipated by Rayleigh friction (not shown).²

We focus on that part of the cascades lying to the left of k_f . As anticipated, there is a net inverse energy cascade. In J1, this tapers off somewhat between k_f and about $k = 30$ and then drops off more quickly between $k = 30$ and $k = 10$. In J2, the initial drop off is less steep (after normalizing for the larger overall magnitude of the flux) and the steeper drop off occurs between roughly $k = 15$ and $k = 8$. As in the gyre experiments, the β and nonlinear components of the flux tend to compensate one another. This is especially evident in J2.

The two-dimensional energy spectra are plotted in Fig. 11. The familiar dumbbell (Vallis and Maltrud, 1993) shaped region which arrests the inverse cascade and is characteristic of the formation of zonal jets is seen in both experiments, but seen more clearly in case J1. Note, however, that the dumbbell is associated with relatively low wavenumbers and the spectra are nearly isotropic in

² This is an artifact of finite resolution. A limited range of wavenumbers separate the forcing scale and the characteristic scale at which dissipation acts. The fraction of energy cascading forward may be estimated as follows: Let ϵ_{uv} be the energy flux that cascades to smaller scales and is dissipated by hyperviscosity and ϵ_{ir} that which inverse-cascades and is ultimately dissipated by Rayleigh friction. Then $\epsilon_{ir} + \epsilon_{uv} = \epsilon$. Further, since the enstrophy and energy input rates are related, $k_{ir}^2 \epsilon_{ir} + k_{uv}^2 \epsilon_{uv} = k_f^2 \epsilon$. Here k_{ir} and k_{uv} are the characteristic wavenumbers at which the large-scale and small-scale dissipations occur. They are estimated by scaling arguments in analogy with that used to obtain the Kolmogorov scale of classical three-dimensional turbulence. For example, k_{ir} may be estimated as follows: $\epsilon_{ir} = r^4 k_{ir}^3 \Rightarrow k_{ir} = \sqrt[3]{\frac{\epsilon}{r^4}}$. From the above equations,

$$\frac{\epsilon_{ir}}{\epsilon_{uv}} = \frac{k_f^2 - k_{uv}^2}{k_{ir}^2 - k_f^2}$$

and is about 2 for the setup considered.

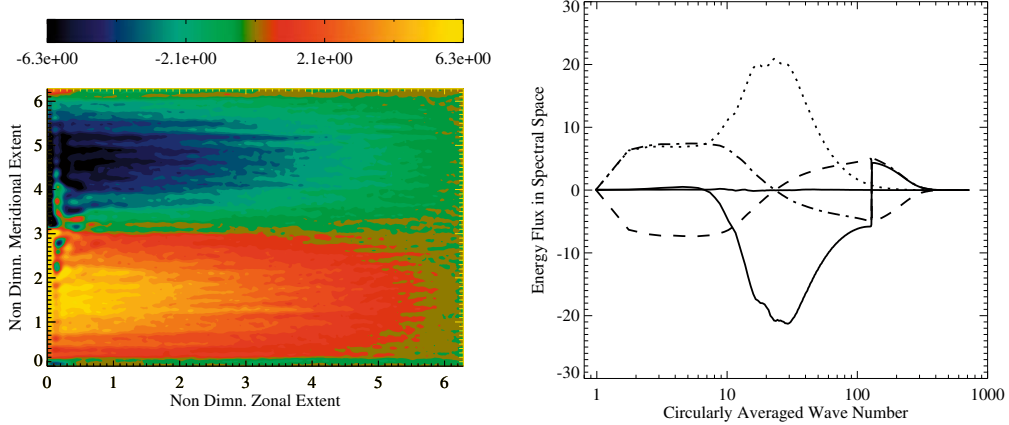


Fig. 12. Experiment G3J1 considers a case with both steady large scale forcing and small scale stochastic forcing. The two forcings are comparable in the sense of the energy flux they drive. $\delta_s = 3.13e - 4$, $\delta_l = 2.97e - 2$, $\delta_i = 5.59e - 3$, $\delta_e = 5.59e - 3$.

the energy-containing wavenumber band – high $kE_{2d}(k)$ – which peaks at about $k \sim 15$ in J1 and $k \sim 10$ in J2. In physical space, this implies that the isotropic eddy field is stronger than the jets, so that the jets are not visible in instantaneous snapshots. An exception to this is that the boundary jets are visible in snapshots of J2. An overall picture of the energetics would then have that about 2/3 of the energy input at k_f is transferred to larger scales by Π_N . Some of this feeds the jets and some is returned to higher k by Π_β . From the two-dimensional energy spectra, however, it seems clear that only a relatively small fraction of the upscale cascade is channeled into the jets. This is unlike in the zonally periodic case and as a result, the jets are apparent only after averaging.

Also shown in Fig. 11 are two-dimensional spectra for G3 and G4. Recall that for these runs, forcing is along the $k_y = 1$ axis and concentrated at low k_x . Relative to J1 and J2, the dumbbell shape appears smaller and the energy-containing wavenumbers display a strong anisotropy, with proportionately less energy in the wavenumbers one would normally associate with jets (i.e., at low k_x and moderate k_y).³ As above, it thus appears that relatively little energy is channeled into the jets which, again, are apparent only after averaging. Note also that for $k_x \sim k_y$ and k_h less than about 20 the two-dimensional spectra show relatively large values. This is particularly evident in G4. Physical space snapshots of fields filtered so as to isolate this part of the spectrum have the appearance of linear Rossby waves with crests oriented at 45° angles to the meridional. It is unclear whether these waves may play a critical role in the enhanced β and nonlinear transfers in the simulations with gyre forcing. Note, however, that similar spectral peaks do not occur in the stochastically forced experiments, for which the enhanced transfers are also present.

3.3. Combined forcing

We now consider the case where both a large scale gyre forcing and a small scale stochastic forcing are applied. As before, we focus on the energy cascades. Since the nonlinear cascade is a third-order quantity, it should give a sensitive measure of interaction. Note, however, that Π in the gyre case typically starts tapering off at relatively small wavenumbers. Conversely, Π in experiments J1 and J2 taper off at relatively large k . As such, it is difficult to find a regime in which the two cascades overlap and therefore one

might anticipate that the interaction will be weak. On the other hand, the β and nonlinear cascades proceed further individually and we can find parameter regimes for which they overlap. We choose G3 as a gyre case that has interesting behavior while remaining in an oceanographically relevant regime. Π in experiment J1 does not overlap significantly with Π in G3; however, there is significant overlap in the individual component cascades. Comparing J2 to G3, the net cascades (Π) show some overlap and the individual components cascades show a large overlap. Note, however, that the fluxes in J2 are significantly stronger than those in G3 since to get the inverse-cascade to proceed to large-scales (at the value of Rayleigh friction for case G3), strong forcing is necessary.

Fig. 12 shows results for experiment G3J1. As anticipated, both the gyres and the jets are clearly visible in the $\bar{\psi}$ field and the nearly compensating β and nonlinear cascades are evident over a range of wavenumbers. Comparing with Figs. 4 and 12, the jets are more evident under combined forcing, as expected. Consistent with this, the magnitudes of the compensating fluxes associated with the jets increases with respect to either case G3 or case J1. Additionally, note that the nonlinear features near the western boundary are more pronounced as is the suggestion of recirculating gyres adjacent to the northern and southern walls. From Fig. 12bb, the strengths of the net forward and inverse cascades (Π) are comparable, although the forward cascade plateaus at a slightly higher value. The zero crossing in Π occurs at about wave-number 20, as do the maxima in the individual component cascades. In experiment G3J2, both the gyres and jets remain evident in $\bar{\psi}$, Fig. 13. Note also that the overall appearance more closely resembles our weakly forced, weakly dissipated experiment (G6) than it does G3. This is perhaps not surprising, given that $\epsilon \gg \bar{W}$ in G3J2. Because of this, the dual (β and nonlinear) cascade is much stronger than the low wavenumber forward cascade associated with the gyre forcing. This was also the case in Experiment G6.

We compared Π_β and Π_N for G3J1 and G3J2 with the linear sum of the corresponding quantities in experiments G3, J1 and J2. If we compare the linear sum to the results under combined forcing, the resulting comparisons are close (not shown). For G3J2, this is perhaps unsurprising, i.e., since $\epsilon \gg \bar{W}$ in this experiment. However, a fairer comparison is perhaps between the G3 fluxes and the difference of the G3J1 and J1 fluxes. This is shown in Fig. 14. In this case, the differences are rather small and the difference can be interpreted as follows: Subtracting the J1 fluxes from the G3J1 fluxes shows compensating β and nonlinear cascades that are slightly stronger and displaced towards smaller wavenumber relative to the fluxes in G3, indicating a slight enhancement of the jets and

³ This is, however, misleading in that the sine transform of a western intensified jet has significant energy at relatively high k_x . For example, the sine transform of a sawtooth in x , $\psi(x, y) = (2\pi - x)$, is given by $\hat{\psi}(k_x) = 2/k_x$, which leads to a white energy spectrum.

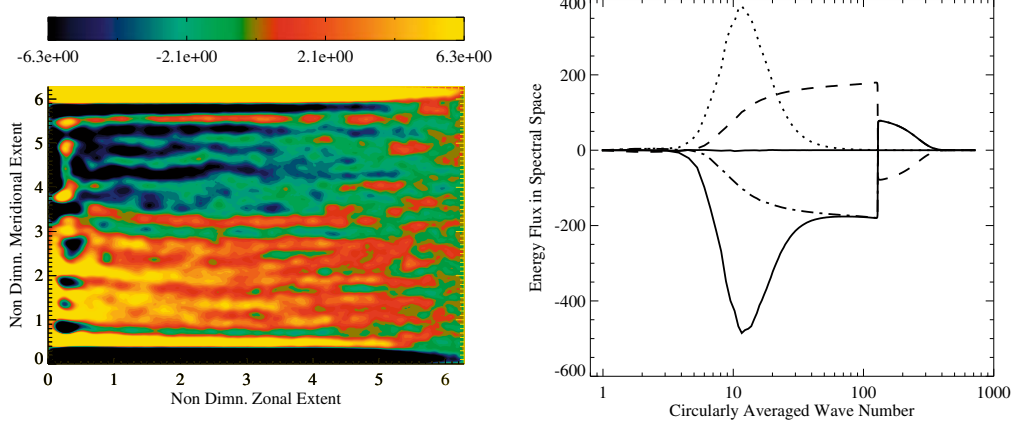


Fig. 13. As in Fig. 9, but for experiment G3J2. $\delta_s = 3.13e-4$, $\delta_l = 2.97e-2$, $\delta_i = 5.59e-3$, $\delta_e = 5.59e-3$.

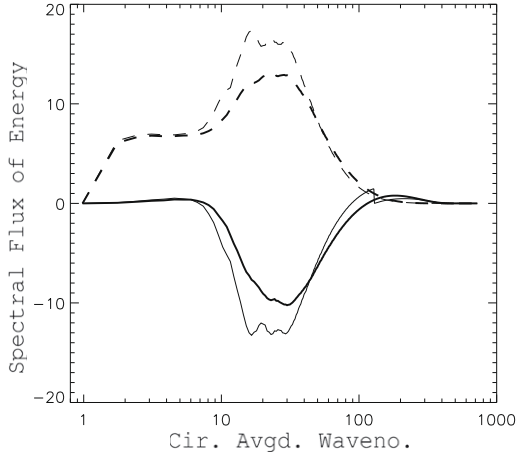


Fig. 14. Comparison of Π_β (dashed lines) and Π_N (continuous lines) for experiment G3 (heavy lines) with the difference of the equivalent fluxes in experiments G3J1 and J1 (lighter lines).

their associated cascades.⁴ In a sense, the relative weakness of the interaction in the G3J1 case is somewhat of a surprise. Note, however, that Π_β and Π_N are both plotted as functions of the angularly averaged horizontal wavenumber. Fig. 15 shows the nonlinear fluxes for G3 and J1 as a function of the meridional wavenumber, k_y .⁵ From the figure, it is clear that Π_N in the gyre case is associated with relatively low k_y , whereas the opposite is true in J1. Evidently, then, the relative lack of interaction has to do with the two cascades occupying different parts of the two-dimensional wavenumber space.

4. Discussion

That the jets are only visible after averaging begs the question of how the jet strength varies with the length of the averaging interval. Moreover, it may also be that the jets are merely an arti-

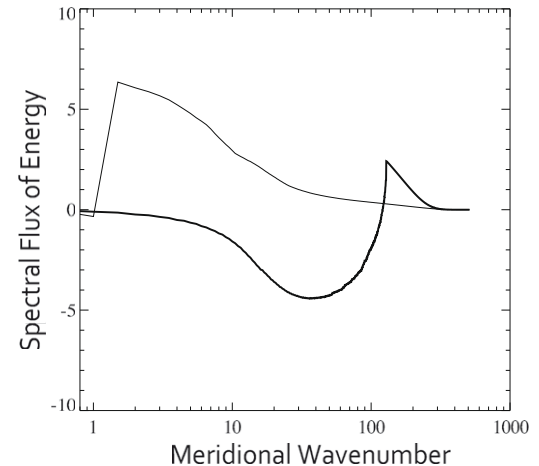


Fig. 15. Π_N averaged over zonal wavenumbers and plotted as a function of the meridional wavenumber for experiments G3 (light line) and J1 (heavy line). That the fluxes for G3 occur at lower meridional wavenumbers than those for J1 is consistent with the relatively weak interaction evidenced in Fig. 14. Note that with averaging over zonal wavenumbers, interpretation in terms of scale interactions is not possible.

fact of averaging together eddies. Indeed this possibility has been suggested as the null hypothesis by Schlaak and Chelton (2008). In the problem they considered, zonal propagation of eddies within a latitude band played a key role. If we instead take the zonally averaged zonal velocity as a measure of the jet strength, propagation within a latitude band does not play a role (i.e., because the position of an eddy within a latitude band has no effect on the eddy's contribution to the zonal average). Note that an instantaneous field of randomly placed eddies would be expected to produce non-zero zonally averaged zonal velocities simply because in a given latitude band the number and strength of positive and negative eddies will not cancel exactly. The average would be positive at some latitudes and negative at others, giving the appearance of jets in the zonally averaged fields. For averaging times, T , long compared to the residence time of a typical eddy within a given latitude band, one expects the rms amplitude of a zonal averages of random eddies to decay like $1/T$.

To remove gyre and boundary contributions to the zonally averaged zonal velocity, a filtering was applied. Define

$$\gamma(y, T, t_0) = \frac{1}{T} \int_{t_0}^{t_0+T} \overline{u^x} dt \quad (4.17)$$

⁴ Similar comparisons of Π_β and Π_N between the G3 fluxes and the difference of the G3J2 and J2 fluxes indicates that the interactions between the jets and the gyre circulations in that case is stronger but is qualitatively in a similar same sense as in G3J1. However, the disparate values of the energy fluxes induced by the jet forcing (large) and the gyre forcing (small) make this comparison rather difficult to assess confidently.

⁵ Note, however, that with this kind of an averaging, as opposed to the previous instances of circular averaging, it is difficult to interpret the fluxes in the sense of dynamics of scale-interactions.

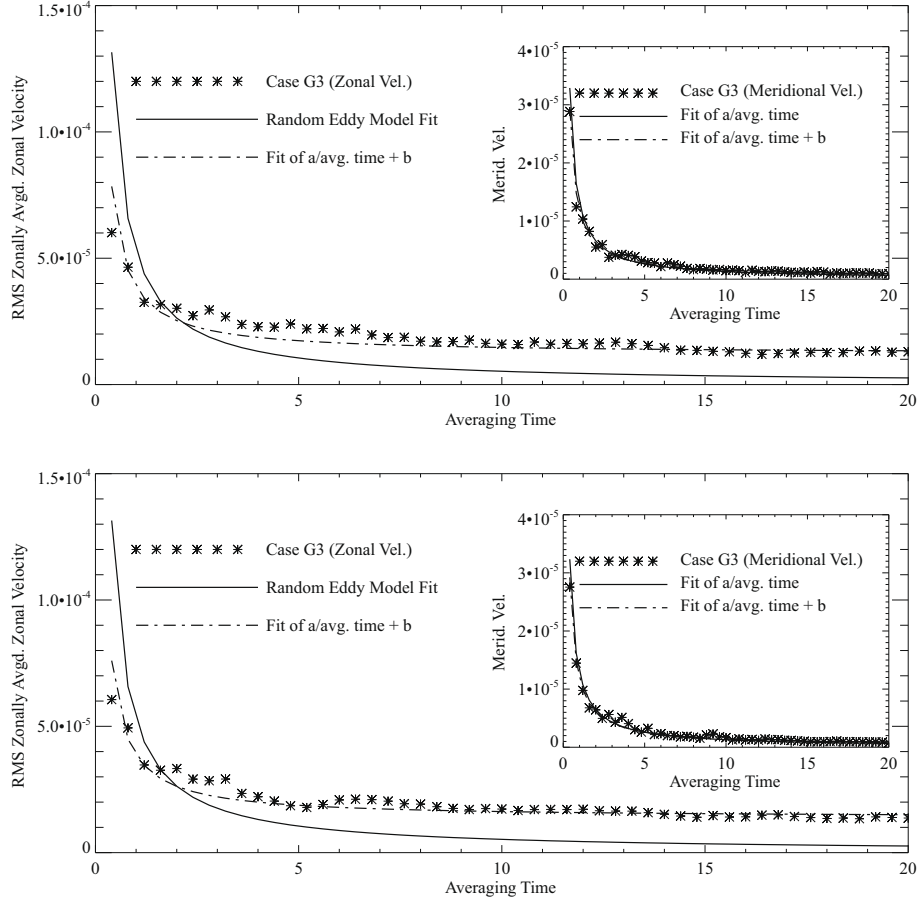


Fig. 16. Amplitude of zonally averaged velocity for experiment G3 (top) and for a twin experiment for which periodicity in y was imposed (bottom). In both cases, a spectral filtering was applied to remove the $k_y = 1$ mode (i.e., corresponding to the gyres) and only the central 60% of the domain in each coordinate direction was considered. Symbols correspond to time averages of the rms value of the zonally averaged zonal velocity and are plotted as a function of the averaging time, T . Solid lines correspond to nonlinear least-squares fits of the random-eddy-model, for which the rms value is inversely proportional to T . Dot-dashed lines correspond to nonlinear least squares fits to a form $a/T + b$, where b represents the jet component (not explained by the random eddies). In the insets are the corresponding analysis for the meridional velocity.

where the overline denotes an x average and superscript f represents the filter. At statistical equilibrium, γ was not strongly dependent on the start time, t_0 , of the averaging interval. Fig. 16 (top) plots the meridional rms value of γ as a function of the averaging time, T . The filter was designed so that u^f is representative of jets and eddies in the interior. First, the $k_y = 1$ mode was removed, so that the diagnostic does not reflect the zonal velocity of the gyres. Next, to eliminate boundary-related effects from the diagnostic, only the central 60% of the domain in each coordinate direction was considered. Finally, a visual inspection (not shown) shows the diagnostic to be a good indicator of the strength of the jets in the middle of the basin. From the figure, there is a clear non-zero offset in the rms jet strength at long times. Specifically, the rms jet strength is better modeled by $a/T + b$ than by a/T , where a and b are constants.

It is interesting to note that meridionally averaging a field of eddies should give rise to apparent meridional jets. Indeed, this is the case in our experiments. The inset of Fig. 16 (top) plots an analog to γ_{rms} , except that γ is defined using meridional averages of the filtered meridional velocity, v^f , and the rms is taken over the zonal direction. From the figure, it is clear that in this case, the strength of meridional averages of v^f clearly tends to zero for large averaging times. That is, the value of b that best fits the data is indistinguishable from zero.

Finally, an analogous diagnostic for our simulations with periodic boundary conditions in y shows remarkably similar results (the lower panel in Fig. 16). This demonstrates that the character-

istics of the interior jets are independent of the presence or absence of the stronger boundary-supported jets. We thus conclude that the zonal jets we see in time averaged fields cannot be considered solely an artifact of averaging random eddies. Rather, they appear to be a weak feature of the flow that is simply not visible in snapshots or short time averages because it is masked by the more energetic eddy field.

The jets appear to be clearly linked to the nonlinear and β dual cascade; however, the precise dynamics leading to this cascade remain somewhat mysterious. One possibility is that the enhanced β transfer is associated with Rossby wave reflection at the western boundary, i.e., since k_x increases upon reflection. In other words, the dual cascade may be related to quasi-linear long waves reflecting into the nonlinear part of the spectrum. Inspection of the transfers did not verify this, however. For example, the β transfers in our gyre experiments generally take energy out of relatively low k_x modes and deposit it at comparable k_y , but larger k_x . These 'source' and 'sink' areas did not, however, lie on or close to opposite sides of the same Rossby wave dispersion curves. That said, it could also be that this discrepancy has to do with the linear dispersion relation not applying near the western boundary.

We also considered the possibility that the enhanced fluxes were due mainly to the strong recirculations appearing adjacent to the northern and southern boundaries. In the main set of experiments, the no normal flow boundary condition there allows for a stronger meridional pressure gradient which can support stronger jets there. We addressed the influence of these boundary-sup-

ported jets on our results in two separate ways. In a first approach, these strong recirculations were removed via a physical space filtering prior to calculating the transfers. This showed Π_β to be reduced, for example, in experiment J2 by about half. From such comparisons, we infer that while the boundary-supported jets account for a significant fraction of the compensating fluxes, a comparable fraction is associated with the interior jets.

In a second approach, a periodicity in y was imposed in the streamfunction and relative vorticity fields across the northern and southern boundaries. Twin experiments, but with the periodic boundary conditions, were performed for cases G3, G4 and G6. Remarkably, we find that the structure and strength of the jets in the interior in these experiments were very similar to our previous results. This suggests that the interior jets are themselves not significantly influenced by the presence of the boundary-supported jets. Rather, they appear as independent features of the flow.

5. Conclusions

We considered the barotropic β -plane vorticity equations under steady large scale and stochastic small scale forcing scenarios. Our principal findings are as follows: (i) in the case with only steady large scale forcing, a weakly forced, weakly dissipated regime is found in which zonal jets appear in time averaged solutions, (ii) coincident with the appearance of the jets is a dual energy cascade in which a linear (β) forward cascade is nearly balanced by the nonlinear inverse energy cascade, (iii) addition of small scale forcing to the gyre problem causes the dual cascade to strengthen and shift towards lower wavenumbers – although the interaction is somewhat weaker than one might have anticipated and, finally, (iv) the jets, as represented by zonally averaged zonal velocities, appear to be a mixture of an averaging artifact of eddies themselves and an underlying jet structure that does not appear to be artefactual.

It is perhaps worth situating our various regimes more clearly with respect to the sorts of parameters typically assumed in the ocean double gyre problem. For example, a 5000 km square basin 5000 m deep forced by a double gyre wind stress such that $\max(\tau)/\rho_0 = 10^{-4}$ m s $^{-2}$ corresponds to a δ_i of about 10^{-2} . Further taking the dimensional Rayleigh drag coefficient to be 10^{-7} s $^{-1}$ gives a δ_l of about 0.04, or about 35% larger than the δ_l in Experiment G3. Alternatively, if one takes the point of view that, since the actual gyre circulation exists mainly in the upper ocean, a smaller depth (e.g., 1000 m) would be more appropriate. This gives values slightly higher values of δ_i and δ_l (e.g., by a factor of $\sqrt{5}$).

Finally, preliminary simulations in a high resolution baroclinic setting show jets to be much more robust (e.g., clearly visible in instantaneous snapshots) than those found here for the barotropic problem. It will be interesting to see whether the jets in the baroclinic gyre problem may also be associated with a near-compensating, dual cascade. In this case, of course, the nonlinear cascade will also involve transfers between vertical wavenumbers.

Acknowledgements

Computational resources were provided under the Institutional Computing initiative at the Los Alamos National Laboratory. Two anonymous reviewers made helpful comments.

Appendix A. Spectra and fluxes in the linear Stommel problem

The steady, linear Stommel double gyre problem has that

$$\beta\psi_x = F_0 \sin(y) - r\psi_{xx}, \quad (5.18)$$

where the Rayleigh drag term has been approximated making use of the fact that the x lengthscale of the boundary current is small com-

pared to the y lengthscale imposed by the forcing. A good approximation to the solution in a square basin of width 2π and for δ_s small is given by

$$\psi = \frac{F_0}{\beta} \sin(y)(x - 2\pi(1 - e^{-\alpha x})), \quad (5.19)$$

where $x = 0$ corresponds to the western boundary and $y = 0$ corresponds to the southern boundary and $\alpha \equiv \delta_s^{-1}$. The Fourier sine transform of ψ , $A(k_x, k_y)$ is zero for all $k_y \neq 1$ and

$$A(k_x, 1) = \frac{F_0}{\beta\pi} \int_0^{2\pi} \sin(k_x x)(x - 2\pi(1 - e^{-\alpha x})) dx, \\ k_x = 1/2, 1, 3/2, \dots \quad (5.20)$$

It is straightforward to show that

$$\frac{F_0}{\beta\pi} \int_0^{2\pi} \sin(k_x x)(x - 2\pi) dx = \frac{-2F_0}{\beta k_x} \quad (5.21)$$

and

$$\frac{2F_0}{\beta} \int_0^{2\pi} \sin(k_x x)e^{-\alpha x} dx = \frac{2F_0 k_x}{\beta(\alpha^2 + k_x^2)}. \quad (5.22)$$

From this it follows that

$$A(k_x, 1) = \frac{-2F_0 \alpha^2}{\beta k_x (\alpha^2 + k_x^2)} \quad (5.23)$$

and the two-dimensional energy spectrum becomes

$$E_{2d}(k_x, 1) = \frac{4F_0^2}{\beta^2} \frac{\alpha^4(1 + k_x^2)}{k_x^2(\alpha^2 + k_x^2)^2}. \quad (5.24)$$

with $E_{2d} = 0$ for $k_y \neq 1$. Then, for $k_x \ll \alpha$,

$$E_{2d}(k_x, 1) \sim 1 + k_x^{-2}. \quad (5.25)$$

so that E_{2d} has its maximum at the gravest wavenumber, $(k_x, k_y) = (1/2, 1)$. Note also that for $k_x \gg 1$,

$$E_{2d}(k_x, 1) \sim \frac{1}{(\alpha^2 + k_x^2)^2}. \quad (5.26)$$

This is approximately constant for $k_x \ll \alpha$ and tapers off like k_x^{-4} at large k_x . Finally, it is of interest to consider $k_x E_{2d}$ and the energy-weighted k_x wavenumber. The former goes like $k_x/(\alpha^2 + k_x^2)^2$ and has a maximum at $\alpha/\sqrt{3}$. For the parameters in Experiment G1, this corresponds to $k_x \approx 93$, which corresponds closely to the maximum slope in Π seen in Fig. 1. The energy-weighted x wavenumber can be estimated as

$$k_e = \frac{\int k_x E(k_x, 1) dk_x}{\int E(k_x, 1) dk_x} \approx \frac{\int_0^\infty k_x (\alpha^2 + k_x^2)^{-2} dk_x}{\int_0^\infty (\alpha^2 + k_x^2)^{-2} dk_x}, \quad (5.27)$$

where the approximation assumes contributions from low k_x to be negligible. Evaluating the integrals, one finds that $k_e \approx 2\alpha/\pi$ or, equivalently, $k_e \approx 2/(\delta_s \pi)$ – which is about 102 for the parameters in G1.

References

- Arakawa, A., 1966. Computational design for long-term numerical integration of the equations of fluid motion: two-dimensional incompressible flow. *i.* Journal of Computational Physics 1 (1), 119–143.
- Berloff, P., 2005. On rectification of randomly forced flows. *Journal of Marine Research* 63 (3), 497–527.
- Berloff, P., Kamenkovich, I., Pedlosky, J., 2009. A mechanism of formation of multiple zonal jets in the oceans. *Journal of Fluid Mechanics* 628, 395–425.
- Connaughton, C., Nadiga, B., Nazarenko, S., Quinn, B., in press. Modulational instability of Rossby and Drift waves and generation of zonal jets. *Journal of Fluid Mechanics*.
- Farrell, B.F., Ioannou, P.J., 2007. Structure and spacing of jets in barotropic turbulence. *Journal of the Atmospheric Sciences* 64 (10), 3652–3665.

- Frisch, U., Kurien, S., Pandit, R., Pauls, W., Ray, S., Wirth, A., Zhu, J., 2008. Hyperviscosity, Galerkin truncation, and bottlenecks in turbulence. *Physical Review Letters* 101 (14), 144501. Available from: <<http://link.aps.org/abstract/PRL/v101/e144501>>.
- Gill, A.E., 1974. The stability of planetary waves on an infinite beta-plane. *Geophysical & Astrophysical Fluid Dynamics* 6, 29.
- Greatbatch, R., Nadiga, B., 2000. Four-gyre circulation in a barotropic model with double-gyre wind forcing. *Journal of Physical Oceanography* 30 (6), 1461–1471. Available from: <<http://public.lanl.gov/balu/nadiga00four.pdf>>.
- Kramer, W., van Buren, M., Clercx, H., van Heijst, G., 2006. Beta-plane turbulence in a basin with no-slip boundaries. *Physics of Fluids* 18 (2), 026603.
- Lorenz, E., 1972. Barotropic instability of Rossby wave motion. *Journal of the Atmospheric Sciences* 29 (2), 258.
- Maximenko, N., Bang, B., Sasaki, H., 2005. Observational evidence of alternating zonal jets in the world ocean. *Geophysical Research Letters* 32 (12), L12607.
- Maximenko, N., Melnichenko, O., Niiler, P., Sasaki, H., 2008. Stationary mesoscale jet-like features in the ocean. *Geophysical Research Letters* 35 (8), L08603.
- Nadiga, B., 2006. On zonal jets in oceans. *Geophysical Research Letters* 33 (10), 4 pp. Available from: <<http://public.lanl.gov/balu/nadiga-06.pdf>>.
- Nakano, H., Hasumi, H., 2005. A series of zonal jets embedded in the broad zonal flows in the pacific obtained in eddy-permitting ocean general circulation models. *Journal of Physical Oceanography* 35 (4), 474–488.
- Panetta, R., 1993. Zonal jets in wide baroclinically unstable regions: persistence and scale selection. *Journal of the Atmospheric Sciences* 50 (14), 2073–2106.
- Pedlosky, J., 1996. *Ocean Circulation Theory*. Springer, Berlin.
- Press, W., Flannery, B., Teukolsky, S., Vetterling, W., 1986. *Numerical recipes, The art of scientific computing*.
- Rhines, P., 1975. Waves and turbulence on a beta-plane. *Journal of Fluid Mechanics* 69, 417–443.
- Richards, K., Maximenko, N., Bryan, F., Sasaki, H., 2006. Zonal jets in the pacific ocean. *Geophysical Research Letters* 33 (3), L03605.
- Salmon, R., 1998. *Lectures on Geophysical Fluid Dynamics*. Oxford University Press, Oxford. p. 378 (Chapter 6).
- Schlax, M.G., Chelton, D.B., 2008. The influence of mesoscale eddies on the detection of quasi-zonal jets in the ocean. *Geophysical Research Letters* 35 (24), L24602.
- Treguier, A., Hogg, N., Maltrud, M., Speer, K., Thierry, V., 2003. The origin of deep zonal flows in the brazil basin. *Journal of Physical Oceanography* 33 (3), 580–599.
- Vallis, G., 2006. *Atmospheric and Oceanic Fluid Dynamics*. Cambridge University Press, Cambridge, MA.
- Vallis, G., Maltrud, M., 1993. Generation of mean flows and jets on a beta-plane and over topography. *Journal of Physical Oceanography* 23 (7), 1346–1362.